Modeling adsorption properties of structurally deformed metal–organic frameworks using structure–property map

WooSeok Jeong[a,1], Dae-Woon Lim[b,1], Sungjune Kim[c], Aadesh Harale[d], Minyoung Yoon[c], Myunghyun Paik Suh[e], and Jihan Kim[a,2]

[a]Department of Chemical and Biomolecular Engineering, Korea Advanced Institute of Science and Technology, Daejeon 34141, Republic of Korea; [b]Division of Chemistry, Graduate School of Science, Kyoto University, Kitashirakawa-Oiwakecho, Sakyo-ku, Kyoto 606–8502, Japan; [c]Department of Nanochemistry, College of Bionano, Gachon University, Sungnam, 13120, Republic of Korea; [d]R&D Center, Saudi Arabian Oil Company, Dhahran 31311, Saudi Arabia; and [e]Department of Chemistry, Seoul National University, Gwanak-gu, Seoul 08826, Republic of Korea

Edited by Omar M. Yaghi, University of California, Berkeley/Lawrence Berkeley National Laboratory, Berkeley, CA, and accepted by Editorial Board Member Tobin J. Marks June 15, 2017 (received for review April 17, 2017)

Structural deformation and collapse in metal-organic frameworks (MOFs) can lead to loss of long-range order, making it a challenge to model these amorphous materials using conventional computational methods. In this work, we show that a structure–property map consisting of simulated data for crystalline MOFs can be used to indirectly obtain adsorption properties of structurally deformed MOFs. The structure–property map (with dimensions such as Henry coefficient, heat of adsorption, and pore volume) was constructed using a large data set of over 12000 crystalline MOFs from molecular simulations. By mapping the experimental data points of deformed SNU-200, MOF-5, and Ni-MOF-74 onto this structure–property map, we show that the experimentally deformed MOFs share similar adsorption properties with their nearest neighbor crystalline structures. Once the nearest neighbor crystalline MOFs for a deformed MOF are selected from a structure–property map at a specific condition, then the adsorption properties of these MOFs can be successfully transformed onto the degraded MOFs, leading to a new way to obtain properties of materials whose structural information is lost.

metal–organic framework | deformation | structure–property map | Monte Carlo simulation | transferability

In the past decade, a large number of metal–organic frameworks (MOFs) have been synthesized for various energy and environmental-related applications (1–3). However, there are many potential drawbacks to these materials that need to be addressed before they can be deployed in real applications. For example, the metal ions and the organic ligands comprising the MOF structures are connected via coordination bonds that can lead to structures that possess both thermal and chemical instabilities (4, 5). As such, MOFs can readily undergo structural transformations under many circumstances, which include various thermal/vacuum treatments on activation, and exposure to air/moisture on handling, leading to irreversible damage (6–9). Although detrimental in most cases, the structural deformation can also be exploited to create strong binding sites that can enhance gas adsorption for sensing/storage purposes (10, 11).

The signs of collapse and deformation of an MOF structure are usually captured by the disappearance, broadening, and/or shift of the powder X-ray diffraction (PXRD) patterns. Unfortunately, the changes observed in the PXRD peaks do not provide detailed information regarding the degree of difference between the examined MOF and its idealized parent, crystalline material. Moreover, for severe degradation where material starts to become increasingly amorphous, it becomes very difficult to model these materials using any of the conventional computational techniques such as molecular simulations due to the absence of structural information.

Here, we present a conceptual platform that uses a large amount of computational data to understand and to indirectly model these deformed, amorphous MOFs even with the lack of structural information. With significant progress being made within the field of computational materials research propelled by the recent White House initiative called the Materials Genome Initiative (12), various research groups have successfully characterized and screened millions of materials in silico, using high-performance computing tools and new methodologies (13–16). With the ever-increasing amount of materials data available to the public, the question of how, when, and where we can use all of this information has not been fully explored by the researchers. Thus far, large-scale in silico screening studies have been mainly used to (*i*) identify the best-performing materials for a given application and (*ii*) elucidate structure/property relationships from large data analysis (13, 15–22). In this work, we report an idea that makes use of a structure–property map constructed using a large number of computational data to indirectly model deformed MOFs in the absence of structural information. Furthermore, the structure–property map is further extended by using the map to detect anomaly experimental data points, illustrating its diverse utility.

Results and Discussion

Construction of a Methane Structure–Property Map. To construct a structure–property map with a large number of simulated data, crystalline structures of experimentally synthesized MOFs, known as the computation-ready, experimental (CoRE) MOF database (i.e., 12,632 fully activated, defect-free, and charge-neutral

Significance

Modeling amorphous materials using the conventional molecular simulation method is exceedingly difficult because structural information of the material is absent. Here, we present a way to indirectly model structurally deformed metal–organic frameworks using a large number of simulation data for crystalline metal–organic frameworks. Our experimental/computational results demonstrate that computed adsorption properties of crystalline metal–organic frameworks can be transferred onto those of structurally deformed, amorphous metal–organic frameworks. This opens up a way to understand adsorption properties of amorphous materials.

Author contributions: J.K. designed research; W.J., D.-W.L., and S.K. performed research; W.J., D.-W.L., A.H., M.Y., M.P.S., and J.K. analyzed data; and W.J., D.-W.L., and J.K. wrote the paper.

The authors declare no conflict of interest.

This article is a PNAS Direct Submission. O.M.Y. is a guest editor invited by the Editorial Board.

[1]W.J. and D.-W.L. contributed equally to this work.

[2]To whom correspondence should be addressed. Email: jihankim@kaist.ac.kr.

This article contains supporting information online at www.pnas.org/lookup/suppl/doi:10.1073/pnas.1706330114/-/DCSupplemental.

3D MOF crystal structures) (23), were used to compute the adsorption properties. With regard to the dimensions of the structure–property map, Henry coefficient (K_H), (zero-coverage isosteric) heat of adsorption (Q_{st}), and (micro)pore volume were selected, as these properties can be obtained readily from experimental isotherm data and can be used to represent adsorption properties of gas molecules across diverse range of pressures: (*i*) Henry coefficient is related with the spatial average accessible density of adsorption sites at specific temperature (24); (*ii*) heat of adsorption represents the (Boltzmann) average binding strength of adsorption sites (1); and (*iii*) micropore volume has a relation to the volume of adsorption sites.

Monte Carlo simulations of 12,632 MOF structures from the CoRE MOF set were conducted using methane as a probe. Methane was chosen due to its industrial importance for storage and separation applications (1, 13, 25, 26). Moreover, methane adsorption in MOFs has been shown to yield relatively accurate data (compared with other polarizable gas molecules), making it an ideal candidate probe to test our methodology (13, 27). From this data set, 6,093 structures with sufficiently large methane adsorption (i.e., $K_H > 10^{-7}$ mol·kg^{-1}·Pa^{-1}) were used to construct the CH_4 structure–property map at $T = 298$ K that consists of heat of adsorption, Henry coefficient, and pore volume (Fig. 1*A*, and see *SI Appendix*, sections 3.1 and 3.2 for details on the calculation). From the structure–property map, clear correlation can be seen among the data points as the CoRE MOF structures that are clustered together in nearby structure–property regions tend to possess similar material properties (e.g., structures with similar K_H and heat of adsorption also tend to have similar pore volumes). This is understandable given that some of these structure–property dimensions are correlated such that it would be very unlikely to find MOFs that simultaneously have extremely high K_H and extremely small heat of adsorption, as an example. To see whether these trends hold for other gas molecules, a structure–property map was obtained from H_2 computational simulations and, similar to CH_4, the general trend of correlation among cluster of points remains the same (*SI Appendix*, Fig. S18).

To examine whether the trend found from the computational structure–property map agrees with the experimental data of crystalline MOFs, 13 experimental data points (1, 28–33) were selected and placed on top of the structure–property map in the 2D view (Fig. 1*B*). The selected experimental data were extracted from recent review papers on methane storage in MOFs (1, 28) and several source papers of the CoRE MOF database (29–33). Except for NU-111, all of the experimental data showed consistent placement within the computational structure–property map. It is noteworthy that adsorption properties for open-metal MOFs (i.e., HKUST-1, UTSA-20, and MOF-74 series) also show consistent property behaviors within the methane structure–property map. It is conceivable that whereas experimental and computational data of the same material might not necessarily agree [e.g., due to the inadequacy of the universal force-field (UFF) model, which is known to give erroneous adsorption energies for open-metal MOFs (34)], the placement within the map showed similar trends.

Building upon this observation, we decided to see what happens upon placing erroneous experimental data onto the structure–property map. As a demonstration, a well-known MOF structure called PCN-14, first synthesized by Ma et al. (35), was chosen as a test case material as it was regarded as a very promising MOF for methane storage with a controversial (at the time) reporting of a significantly large methane heat of adsorption (30 kJ/mol). Subsequent experimental studies conducted by Peng et al. (36) and Mason et al. (1) showed that the heat of adsorption values were significantly smaller [17.6 kJ/mol (Mason et al.), 18.7 kJ/mol (Peng et al.)] compared with what was reported in the original paper. With the placement of these three data points onto the methane structure–property map from the previous section, it can be clearly seen that the original PCN-14 is an anomaly point (Fig. 1*C*). Subsequently, one important utility of our computational structure–property map is that it can potentially be used to detect experimental errors that might not be apparent without the proper context of large amounts of data. This can allow

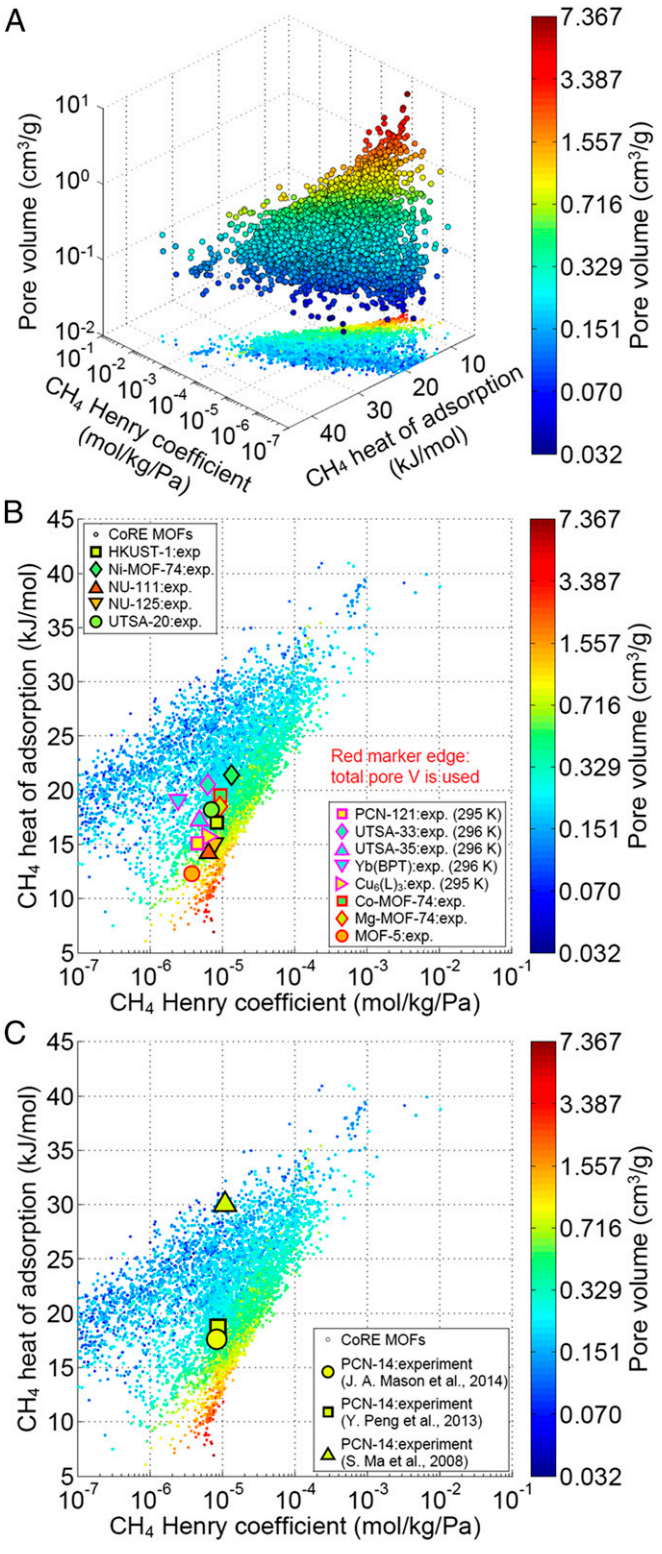

Fig. 1. (*A*) CH_4 structure–property map at 298 K constructed using the simulated adsorption data of the CoRE MOFs (6,093 structures, which show CH^4 $K_H > 10^{-7}$ mol·kg^{-1}·Pa^{-1}). The projected data are displayed in the bottom of the graph. Experimental data are placed on top of the map: (*B*) crystalline MOF structures, and (*C*) multiple PCN-14 structures.

experimentalists to input their experimental data point on a preexisting structure–property map to determine the veracity of their own work.

Adsorption Properties of Deformed MOFs on the Structure–Property Map. Next, we moved to the degraded MOFs to examine whether the MOFs that have lost their crystallinity still showed similar trends within our computational structure–property map. SNU-200, MOF-5, and Ni-MOF-74 were selected as test materials to develop our method. N_2 isotherms at $T = 77$ K and CH_4 isotherms at $T = 298$ K were obtained from our experiments. As shown in the adsorption isotherms of *SI Appendix*, Fig. S7, in the case of MOF-5 and Ni-MOF-74 the MOFs were degraded gradually from exposure to air at varying times.

A total of 13 experimental data points of these parent/deformed MOFs at $T = 298$ K were positioned onto the CH_4 structure–property map, as shown in Fig. 2*A*. By tracing the path of air exposure from 0 to 24 h for the two MOFs within the structure–property space, different trends can be identified. For MOF-5, there is (*a*) decreasing K_H; (*b*) increasing heat of methane adsorption; and (*c*) decreasing pore volume. Upon structural deformation, the reduction in the pore volume is most likely accompanied by creation of strong adsorption sites that might be responsible for the enhanced heat of methane gas adsorption. For Ni-MOF-74, compared with MOF-5, relatively smaller changes were observed perhaps due to the environment around the open-metal sites that remains largely the same during air exposure.

What is interesting from Fig. 2*A* is that the pore volumes of all of the degraded MOFs on the CH_4 structure–property map showed good agreement with the values from the nearby CoRE MOF structures. To test the robustness of this observation, the dimensions/conditions were changed in the following manner to create different structure–property maps: (*i*) temperature was changed from $T = 298$ to 195 K and computational and experimental data were both collected at $T = 195$ K for all of the MOF structures (Fig. 2*B*) and (*ii*) the structure–property dimension of pore volume was changed to the methane uptake value at 1 bar (Fig. 2*C*). In all of these cases, strong correlation between the properties of the parent/deformed and the crystalline MOFs remains intact. These results indicate that structurally deformed MOFs fundamentally share similar sets of properties compared with crystalline MOFs that are located nearby in the structure–property map. This is not a priori obvious as there are instances (e.g., PCN-14 with experimental error) where structures need not share similar properties with nearby neighbors. The implication here is that it is conceivable the material properties (e.g., Henry's constant, heat of adsorption, and pore volume) of crystalline MOFs can potentially be transferred to those of the deformed materials if judiciously selected.

Transferability of Structure–Property Maps. To verify the aforementioned claim, the CoRE MOF structures that are most similar to each of the 13 experimental MOF data points were identified in the CH_4 structure–property map (Fig. 2*A*). To quantify similarity, the Euclidean distance of the normalized methane structure–property map at $T = 298$ K was used. Specifically, the max–min normalization (Eq. **1**) was adopted due to its simplicity on eliminating different physical units of dimensions.

$$y_{norm} = \frac{y_{original} - y_{min}}{y_{max} - y_{min}}, \qquad [1]$$

where y_{norm} is the transformed property value through the max–min normalization, $y_{original}$ is the original property value of interest (e.g., experimental data for deformed MOFs), and y_{min} and y_{max} are the minimum and maximum values of the properties in the structure–property map. By using these unitless adsorption properties from the normalized CH_4 structure–property map, the Euclidean distances between experimental data of 13 of the parent/deformed MOFs and all of the CoRE MOF simulated

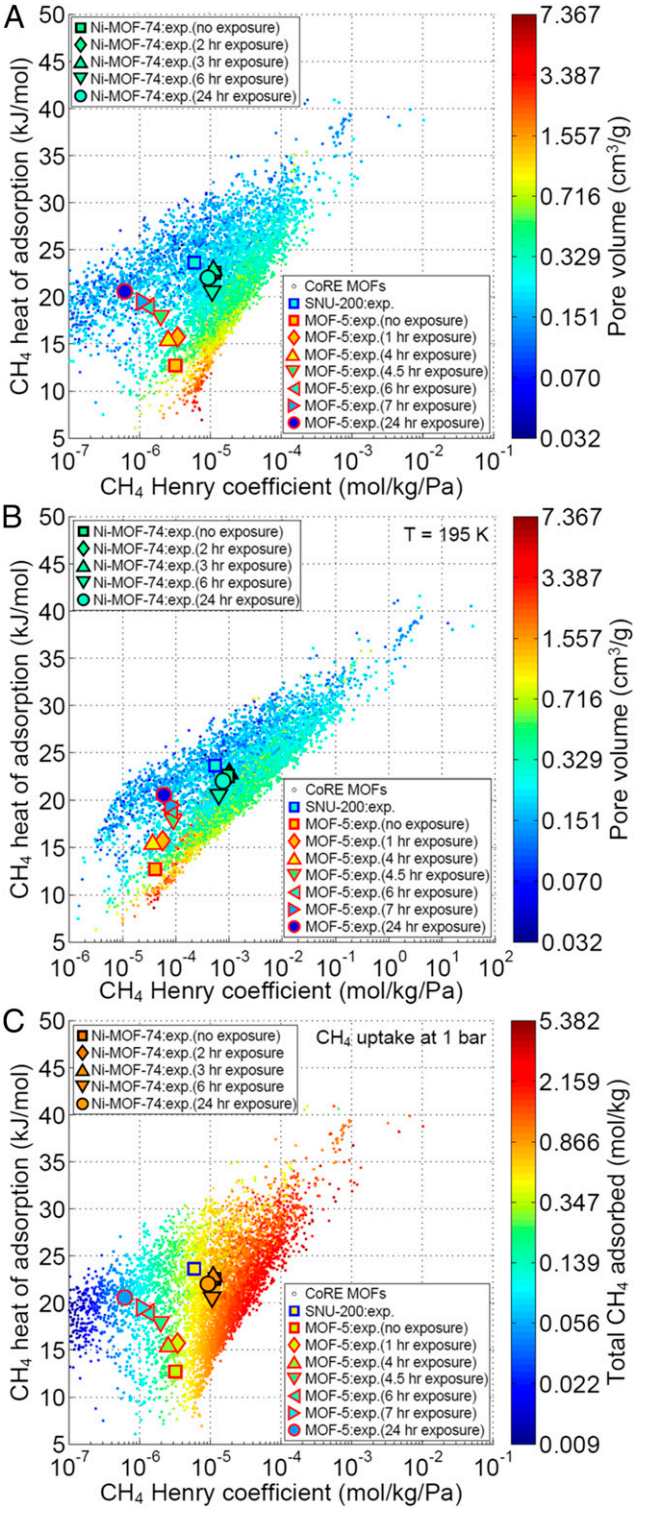

Fig. 2. CH_4 structure–property maps with the experimental adsorption data of the deformed SNU-200, MOF-5, and Ni-MOF-74 samples. Experimental data are placed on top of the map with the following structure–property dimensions: (*A*) ($T = 298$ K) CH_4 Henry's constant, CH_4 heat of adsorption, and pore volume; (*B*) ($T = 195$ K) CH_4 Henry's constant, CH_4 heat of adsorption, and pore volume; and (*C*) ($T = 298$ K) CH_4 Henry's constant, CH_4 heat of adsorption, and CH_4 uptake at 1 bar.

data were computed. Next, the 5 closest crystalline MOF structures for each of the 13 experimental data points were selected as the nearest-neighbor MOFs (*SI Appendix*, Fig. S10). Five is an arbitrary number that we have chosen and our analysis has shown that changing this number does not change the overall conclusion (see *SI Appendix*, section 3.3 for results with 1, 3, 5, 8, 10, 20, and 30 nearest-neighboring MOFs).

Computational simulations were conducted on these nearest CoRE MOF structures ($5 \times 13 = 65$ structures altogether) using the methane and the hydrogen probes over a wide range of temperatures ($T = 77$ to 313 K), with corresponding 52 experimental data collected for the 13 parent/deformed MOFs (*SI Appendix*, Tables S4, S5, and S8). Comparisons between the computational properties (calculated by taking the averages of K_H, heat of gas adsorption, and pore volume) of the five similar MOFs and the corresponding experimental data indicate that across a wide range of structures and temperatures that have undergone varying degrees of deformation, the overall agreement is very good (Fig. 3). It is noteworthy that H_2 data (at $T = 77$ and 87 K, Fig. 3) show good agreement between the simulation and the experimental data as well, signifying that transferability works across different gas molecules.

Accordingly, if we were given a single set of experimental data at a specific condition (e.g., methane adsorption properties at $T = 298$ K) for a degraded MOF, the nearest-neighbor crystalline materials could be identified from a structure–property map and their adsorption properties could be successfully transferred onto these deformed materials at different conditions (*SI Appendix*, section 5.2).

The utility of transferability can be significant given that certain material properties (e.g., gas molecule binding energy and gas molecule potential energy distributions) simply cannot be obtained in the absence of the structure information. For example, methane potential energy histograms for five nearest-neighbor MOFs of the degraded MOF-5 structures with different humid air treatments are similar to one another (Fig. 4 and *SI Appendix*, section 3.4). Thus, these data provide quantitative insights into the energetics of the pores and can only be obtained via simulations (it is not possible to get these data via experiments) of the similar crystalline materials.

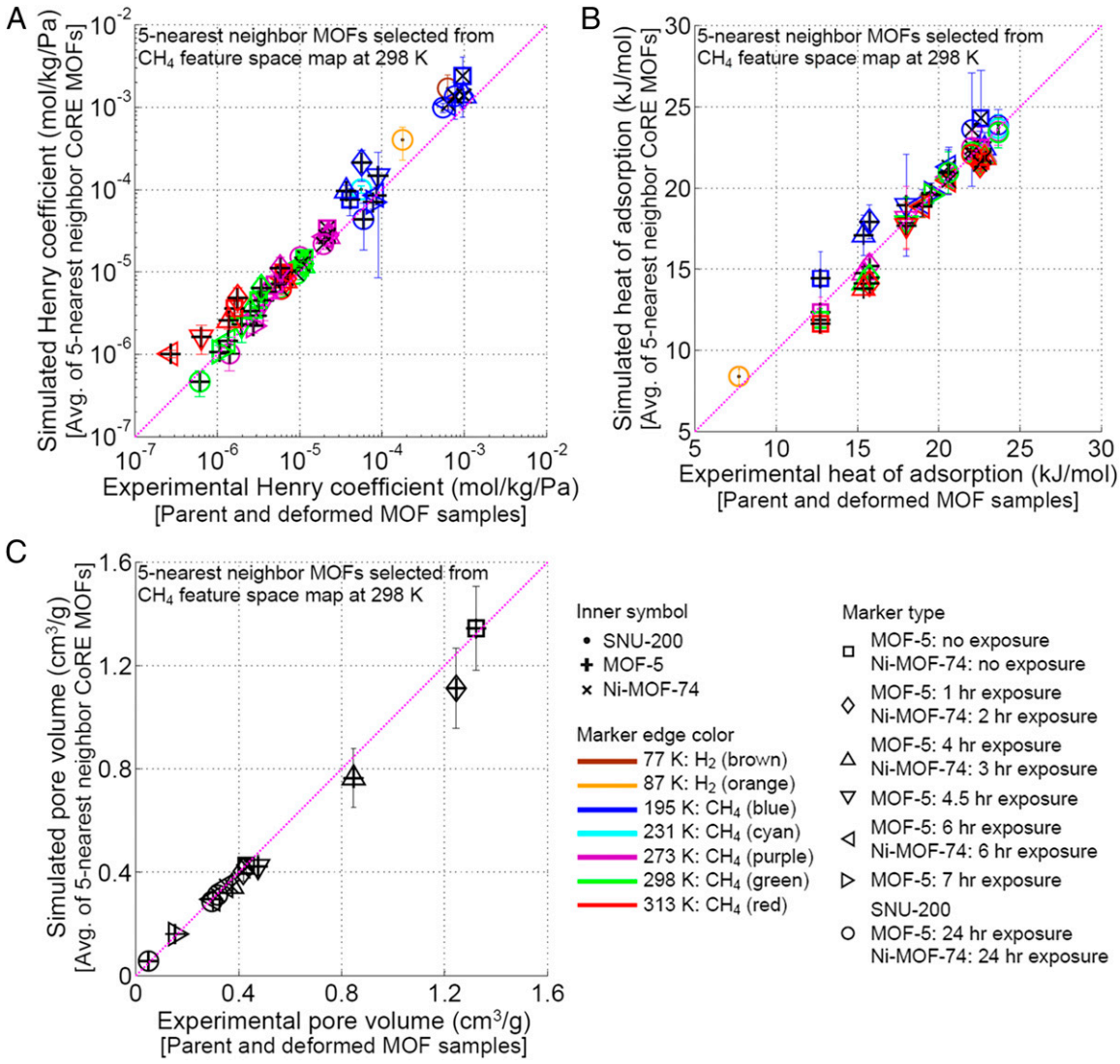

Fig. 3. Property transferability test between experimental data of the structurally deformed MOFs (SNU-200, MOF-5, and Ni-MOF-74) and computational data with the simulated properties taken from the average values of the five nearest-neighbor crystalline CoRE MOFs in the CH_4 structure–property map at 298 K for (*A*) CH_4 Henry coefficient, (*B*) CH_4 heat of adsorption, and (*C*) pore volume. The purple line ($y = x$) indicates a region where there is perfect agreement between experimental and simulated data. The error bar arises from the SD of the five nearest-neighbor values.

In particular, the energetics of the pores analyzed from the CH_4 energy histograms can also be used to understand the deformation behaviors of the degraded MOFs. As the exposure time to air increases for the MOF-5 samples, increasing numbers of strong binding sites (i.e., the appearance of the frequency of the lower CH_4 energies) are created as can be seen from the energy histograms, resulting in a higher heat of adsorption for CH_4. However, the density of favorable binding sites, which has a negative CH_4 energy value, diminishes significantly along with the air exposure time from 4-h air exposure to 4.5-h exposure.

Conclusions

In summary, structure–property relationship analysis provides evidence that both crystalline and structurally deformed MOFs share similar trends within the map as demonstrated by the comparisons between the deformed SNU-200/MOF-5/Ni-MOF-74 structures and their nearest-neighbor CoRE MOF data points. Accordingly, we have used this observation to hypothesize and to demonstrate transferability between the adsorption properties of these deformed MOFs and those of the nearest-neighbor crystalline structures within the structure–property map, opening up a conceptual platform to understand and to indirectly obtain adsorption properties of these deformed materials. At this point, we acknowledge that it is unclear where the concept of transferability breaks down. For example, for completely different guest molecules (e.g., CO_2 or long alkanes), the transferability might not hold. However, we hypothesize that this "limitation" can be addressed by including more dimensions in the original structure–property space such that structures become more similar across a larger number of structure–property dimensions.

The utility of the structure–property relationship analysis can be extended to other avenues in which we show that reliability of experimental data can be readily checked. Also, adsorption experiments at harsh and/or specific conditions (e.g., radioactive, toxic, and/or explosive gas, at cryogenic temperatures), might be difficult to perform in a general laboratory setting, and thereby our method can facilitate producing relevant data. The ideas that we have developed can perhaps be generalized to not only deformed MOF structures, but also other materials (e.g., polymers, carbonaceous materials) that are known to be more amorphous. With the ever-increasing amount of available experimental and computational porous materials data, it is our current vision that more advanced and sophisticated structure–property relationships can help us better understand and to model materials in which structure information is unknown or incomplete.

Materials and Methods

Experimental Structural Deformation of MOFs. SNU-200 was selected as it was initially synthesized by a few of the authors in this paper, and disappearance, broadening, and shift of the PXRD peaks were observed upon activation of the as-synthesized SNU-200 with supercritical CO_2 (37), indicating signs of structural collapse. The deformed SNU-200 sample was prepared according to the previous report (*SI Appendix*, section S1.2). MOF-5 (38) and Ni-MOF-74 (39) were selected as representative materials for analysis as they are some of the most well-known and commonly studied MOFs. MOF-5 and Ni-MOF-74 were artificially degraded by controlling air exposure time of the samples with 40% humidity at room temperature from 0 to 24 h. To obtain methane adsorption data, low-pressure (up to 1 bar) isotherm experiments were conducted for SNU-200 (at 195, 231, 273, and 298 K), and all of the samples of MOF-5 and Ni-MOF-74 (at 195, 273, 298, and 313 K). N_2 isotherms at $T = 77$ K were performed for all of the MOF samples and the Dubinin and Radushkevich (DR) method (40) was used to obtain the micropore volume (see *SI Appendix*, section 4 for details). If N_2 uptakes at low pressures, which are required to obtain micropore

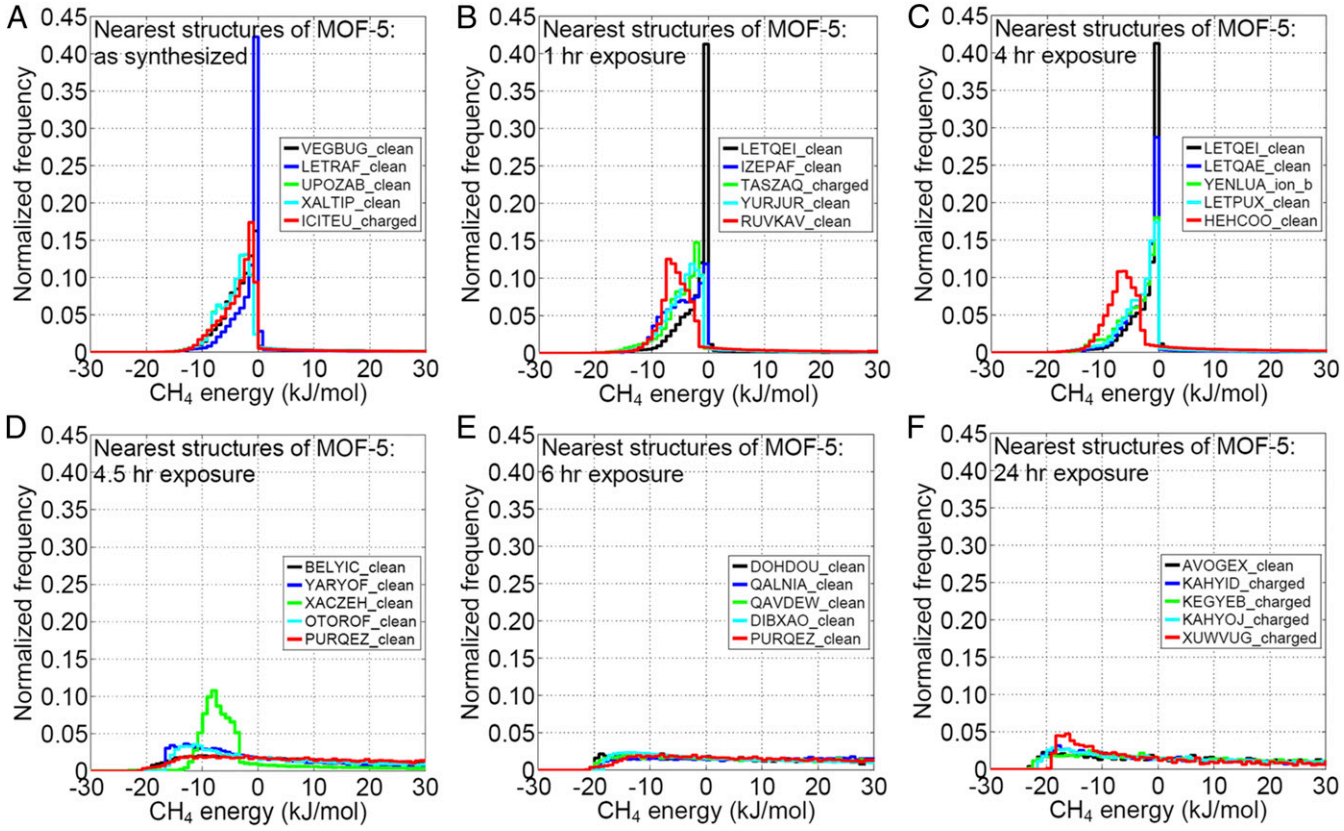

Fig. 4. CH_4 energy histograms of each of the five nearest-neighbor CoRE MOFs in the CH_4 structure–property map at 298 K for the MOF-5 samples with different level of air treatments. (*A*) 0 h, (*B*) 1 h, (*C*) 4 h, (*D*) 4.5 h, (*E*) 6 h, and (*F*) 24 h.

volume using the DR method, are not available, total pore volumes reported in the previous work were used because total pore volume is almost the same as the micropore volume for a crystalline microporous MOF. Before gas sorption measurements, the air-exposed samples were evacuated at 373 K for reactivation.

Monte Carlo Simulations. Henry coefficients and heats of adsorption were obtained using the Widom insertion Monte Carlo method. Grand canonical Monte Carlo simulations were performed to obtain the adsorption isotherms data (41, 42). To accelerate the simulations, an in-house graphics-processing-unit–based code (43, 44) was used with an energy grid with a grid spacing of 0.15 Å. The interaction energies between the gas molecule and the framework atoms were calculated using the 12–6 Lennard-Jones (LJ) potential model with a cutoff radius of 12.8 Å with the Lorentz–Berthelot mixing rule. The UFF (45) was used to model the framework atoms as it has been shown that the UFF can accurately model CH_4 and H_2 uptakes for various MOFs (27, 46). At low temperatures (T = 77 and 87 K), the Feynman–Hibbs effective potential (47, 48) was used to correct the quantum effects for the hydrogen. The Buch LJ potentials (49) and the TraPPE force fields (50) were adopted for H_2 and CH_4, respectively. Here, Widom insertion moves of 35,000,000 were performed for each structure to obtain accurate simulation results.

ACKNOWLEDGMENTS. The authors gratefully acknowledge the financial support from the Saudi Aramco-Korea Advanced Institute of Science and Technology CO_2 Management Center. This research used resources of the National Energy Research Scientific Computing Center, a Department of Energy (DOE) Office of Science User Facility Supported by the Office of Science of the US DOE under Contract DE-AC02-05CH11231.

1. Mason JA, Veenstra M, Long JR (2014) Evaluating metal-organic frameworks for natural gas storage. *Chem Sci (Camb)* 5:32–51.
2. Furukawa H, Cordova KE, O'Keeffe M, Yaghi OM (2013) The chemistry and applications of metal-organic frameworks. *Science* 341:1230444.
3. Suh MP, Park HJ, Prasad TK, Lim D-W (2012) Hydrogen storage in metal-organic frameworks. *Chem Rev* 112:782–835.
4. Bosch M, Zhang M, Zhou H-C (2014) Increasing the stability of metal-organic frameworks. *Adv Chem* 2014:8.
5. Howarth AJ, et al. (2016) Chemical, thermal and mechanical stabilities of metal–organic frameworks. *Nat Rev Mater* 1:15018.
6. Guo P, Dutta D, Wong-Foy AG, Gidley DW, Matzger AJ (2015) Water sensitivity in Zn_4O-based MOFs is structure and history dependent. *J Am Chem Soc* 137:2651–2657.
7. Burtch NC, Jasuja H, Walton KS (2014) Water stability and adsorption in metal-organic frameworks. *Chem Rev* 114:10575–10612.
8. DeCoste JB, et al. (2013) The effect of water adsorption on the structure of the carboxylate containing metal-organic frameworks Cu-BTC, Mg-MOF-74, and UiO-66. *J Mater Chem A Mater Energy Sustain* 1:11922–11932.
9. Kaye SS, Dailly A, Yaghi OM, Long JR (2007) Impact of preparation and handling on the hydrogen storage properties of Zn_4O(1,4-benzenedicarboxylate)$_3$ (MOF-5). *J Am Chem Soc* 129:14176–14177.
10. Fang Z, Bueken B, De Vos DE, Fischer RA (2015) Defect-engineered metal–organic frameworks. *Angew Chem Int Ed Engl* 54:7234–7254.
11. Gadipelli S, Guo Z (2014) Postsynthesis annealing of MOF-5 remarkably enhances the framework structural stability and CO_2 uptake. *Chem Mater* 26:6333–6338.
12. US Office of Science and Technology Policy (2011) Materials genome initiative: A renaissance of American manufacturing. Available at https://obamawhitehouse.archives.gov/blog/2011/06/24/materials-genome-initiative-renaissance-american-manufacturing. Accessed July 1, 2016.
13. Simon CM, et al. (2015) The materials genome in action: Identifying the performance limits for methane storage. *Energy Environ Sci* 8:1190–1199.
14. Jain A, et al. (2013) Commentary: The materials project: A materials genome approach to accelerating materials innovation. *APL Mater* 1:011002.
15. Wilmer CE, et al. (2011) Large-scale screening of hypothetical metal-organic frameworks. *Nat Chem* 4:83–89.
16. Lin L-C, et al. (2012) In silico screening of carbon-capture materials. *Nat Mater* 11:633–641.
17. Kwon O, Park S, Zhou H-C, Kim J (2017) Computational prediction of heterointerpenetration in metal-organic frameworks. *Chem Commun (Camb)* 53:1953–1956.
18. Li S, Chung YG, Snurr RQ (2016) High-throughput screening of metal–organic frameworks for CO_2 capture in the presence of water. *Langmuir* 32:10368–10376.
19. Jeong W, Kim J (2016) Understanding the mechanisms of CO_2 adsorption enhancement in pure silica zeolites under humid conditions. *J Phys Chem C* 120:23500–23510.
20. Banerjee D, et al. (2016) Metal–organic framework with optimally selective xenon adsorption and separation. *Nat Commun* 7:ncomms11831.
21. Martin RL, et al. (2014) In silico design of three-dimensional porous covalent organic frameworks via known synthesis routes and commercially available species. *J Phys Chem C* 118:23790–23802.
22. Kim J, et al. (2013) New materials for methane capture from dilute and medium-concentration sources. *Nat Commun* 4:1694.
23. Chung YG, et al. (2014) Computation-ready, experimental metal–organic frameworks: A tool to enable high-throughput screening of nanoporous crystals. *Chem Mater* 26:6185–6192.
24. Do DD, Nicholson D, Do HD (2008) On the Henry constant and isosteric heat at zero loading in gas phase adsorption. *J Colloid Interface Sci* 324:15–24.
25. Mason JA, et al. (2015) Methane storage in flexible metal-organic frameworks with intrinsic thermal management. *Nature* 527:357–361.
26. Jensen NK, et al. (2012) Screening zeolites for gas separation applications involving methane, nitrogen, and carbon dioxide. *J Chem Eng Data* 57:106–113.
27. McDaniel JG, Li S, Tylianakis E, Snurr RQ, Schmidt JR (2015) Evaluation of force field performance for high-throughput screening of gas uptake in metal–organic frameworks. *J Phys Chem C* 119:3143–3152.
28. He Y, Zhou W, Qian G, Chen B (2014) Methane storage in metal-organic frameworks. *Chem Soc Rev* 43:5657–5678.
29. Park J, Li J-R, Sañudo EC, Yuan D, Zhou H-C (2012) A porous metal-organic framework with helical chain building units exhibiting facile transition from micro- to mesoporosity. *Chem Commun (Camb)* 48:883–885.
30. Li C, et al. (2012) A pcu-type metal-organic framework based on covalently quadruple cross-linked supramolecular building blocks (SBBs): Structure and adsorption properties. *CrystEngComm* 14:1929–1932.
31. He Y, et al. (2012) A robust doubly interpenetrated metal-organic framework constructed from a novel aromatic tricarboxylate for highly selective separation of small hydrocarbons. *Chem Commun (Camb)* 48:6493–6495.
32. He Y, et al. (2012) A microporous metal-organic framework for highly selective separation of acetylene, ethylene, and ethane from methane at room temperature. *Chemistry* 18:613–619.
33. Guo Z, et al. (2011) A robust near infrared luminescent ytterbium metal-organic framework for sensing of small molecules. *Chem Commun (Camb)* 47:5551–5553.
34. Fischer M, Gomes JRB, Jorge M (2014) Computational approaches to study adsorption in MOFs with unsaturated metal sites. *Mol Simul* 40:537–556.
35. Ma S, et al. (2008) Metal-organic framework from an anthracene derivative containing nanoscopic cages exhibiting high methane uptake. *J Am Chem Soc* 130:1012–1016.
36. Peng Y, et al. (2013) Methane storage in metal-organic frameworks: Current records, surprise findings, and challenges. *J Am Chem Soc* 135:11887–11894.
37. Lim D-W, Chyun SA, Suh MP (2014) Hydrogen storage in a potassium-ion-bound metal-organic framework incorporating crown ether struts as specific cation binding sites. *Angew Chem Int Ed Engl* 53:7819–7822.
38. Li H, Eddaoudi M, O'Keeffe M, Yaghi OM (1999) Design and synthesis of an exceptionally stable and highly porous metal-organic framework. *Nature* 402:276–279.
39. Caskey SR, Wong-Foy AG, Matzger AJ (2008) Dramatic tuning of carbon dioxide uptake via metal substitution in a coordination polymer with cylindrical pores. *J Am Chem Soc* 130:10870–10871.
40. ISO 15901-3 (2007) Pore size distribution and porosity of solid materials by mercury porosimetry and gas adsorption – Part 3: Analysis of micropores by gas adsorption (ISO, Geneva).
41. Smit B, Maesen TLM (2008) Molecular simulations of zeolites: Adsorption, diffusion, and shape selectivity. *Chem Rev* 108:4125–4184.
42. Frenkel D, Smit B (2001) *Understanding Molecular Simulation: From Algorithms to Applications* (Academic, London).
43. Kim J, Martin RL, Rübel O, Haranczyk M, Smit B (2012) High-throughput characterization of porous materials using graphics processing units. *J Chem Theory Comput* 8:1684–1693.
44. Kim J, Rodgers JM, Athènes M, Smit B (2011) Molecular Monte Carlo simulations using graphics processing units: To waste recycle or not? *J Chem Theory Comput* 7:3208–3222.
45. Rappe AK, Casewit CJ, Colwell KS, Goddard WA, Skiff WM (1992) UFF, a full periodic table force field for molecular mechanics and molecular dynamics simulations. *J Am Chem Soc* 114:10024–10035.
46. Basdogan Y, Keskin S (2015) Simulation and modelling of MOFs for hydrogen storage. *CrystEngComm* 17:261–275.
47. Tchouar N, Ould-Kaddour F, Levesque D (2004) Computation of the properties of liquid neon, methane, and gas helium at low temperature by the Feynman-Hibbs approach. *J Chem Phys* 121:7326–7331.
48. Guillot B, Guissani Y (1998) Quantum effects in simulated water by the Feynman–Hibbs approach. *J Chem Phys* 108:10162–10174.
49. Buch V (1994) Path integral simulations of mixed para-D_2 and ortho-D_2 clusters: The orientational effects. *J Chem Phys* 100:7610–7629.
50. Martin MG, Siepmann JI (1998) Transferable potentials for phase equilibria. 1. United-atom description of n-alkanes. *J Phys Chem B* 102:2569–2577.